Bulletin of Volcanology (2019) 81:22
https://doi.org/10.1007/s00445-019-1283-z

RESEARCH ARTICLE

Experimental constraints on the textures and origin of obsidian pyroclasts

James E. Gardner[1] · Fabian B. Wadsworth[2] · Edward W. Llewellin[2] · James M. Watkins[3] · Jason P. Coumans[2]

Received: 13 September 2018 / Accepted: 22 February 2019

Abstract
Obsidian pyroclasts are commonly preserved in the fall deposits of explosive silicic eruptions. Recent work has suggested that they form by sintering of ash particles on the conduit walls above the fragmentation depth and are subsequently torn out and transported in the gas-particle dispersion. Although the sintering hypothesis is consistent with the general vesicle textures and dissolved volatiles in obsidian pyroclasts, previous sintering experiments do not capture all of the textural complexities observed in the natural pyroclasts. Here, we design experiments in which unimodal and bimodal distributions of rhyolitic ash are sintered at temperatures and H_2O pressures relevant to shallow volcanic conduits and under variable cooling rates. The experiments produce dense, welded obsidian that have a range of textures similar to those observed in natural pyroclasts. We find that using a unimodal distribution of particles produces obsidian with evenly distributed trapped vesicles, while a bimodal initial particle distribution produces obsidian with domains of poorly vesicular glass among domains of more vesicle-rich glass. We also find that slow cooling leads to resorption of trapped vesicles, producing fully dense obsidian. These broad features match those found in obsidian pyroclasts from the North Mono (California, USA) rhyolite eruption, providing strong support to the hypothesis that obsidian can be produced by ash sintering above the fragmentation depth during explosive eruptions.

Keywords Obsidian · Ash · Sinter · Volatile · Explosive eruption

Introduction

Obsidian pyroclasts—pieces of glassy rhyolite found in tephra deposits—have played a central role in the development of models for silicic magma degassing and volcanic eruptions. Found in most rhyolitic tephras that are associated with domes or lavas (e.g., Rust et al. 2004; Castro et al. 2014; Watkins et al. 2017; Gardner et al. 2017), these pyroclasts record a wide range of dissolved volatile contents, all of which are partially degassed relative to initial storage conditions (Taylor et al. 1983; Newman et al. 1988; Taylor 1991; Watkins et al. 2017). This observation, combined with their low-to-zero vesicularity, was first explained by what became known as the "permeable foam model," in which bubbly rhyolitic magma becomes permeable through partial bubble coalescence, allowing gases to escape and the remnant magma to collapse to a bubble-poor melt (Eichelberger et al. 1986; Jaupart and Allegre 1991). This paradigm was linked to eruptive style, such that the collapse of the foam was postulated to cause the magma to effuse as degassed lava instead of erupting explosively (Eichelberger et al. 1986). More recent models have been proposed to explain the high dissolved volatile contents that appear inconsistent with the permeable foam model (e.g., Rust et al. 2004; Gonnermann and Manga 2005a, b; Okumura et al. 2009; Cabrera et al. 2011; Castro et al. 2014). Textural evidence for brittle behavior in otherwise hot, viscous silicic magma has been used to implicate fracturing as the cause of open-system behavior (Tuffen et al. 2003; Tuffen and Dingwell 2005; Cabrera et al. 2011), which in turn appears consistent with the style and extent of degassing recorded by dissolved volatiles (Rust et al. 2004; Castro et al. 2014). These models converge on the idea that brittleness

Editorial responsibility: M.I. Bursik

✉ James E. Gardner
gardner@mail.utexas.edu

[1] Department of Geological Sciences, Jackson School of Geosciences, The University of Texas at Austin, Austin, TX 78712-0254, USA

[2] Department of Earth Sciences, Science Labs, Durham University, Durham DH1 3LE, UK

[3] Department of Earth Sciences, University of Oregon, Eugene, OR 97403-1272, USA

resulting from high local strain rates in the melt leads to fractures that open the system and that this fracturing occurs repetitively (Tuffen et al. 2003) and pervasively (Castro et al. 2012) during magma ascent.

Gardner et al. (2017) re-examined obsidian pyroclasts from the North Mono eruption and found multiple lines of evidence that the obsidian is not collapsed foam. Instead, they proposed a model in which volcanic ash travelling up the conduit, above the fragmentation level, sticks to conduit walls and sinters to form low-porosity melt. Blebs of this melt are then reincorporated into the eruption to be deposited as glassy pyroclasts in the mainly pumiceous tephra. In this framework, variations in dissolved volatile concentrations represent differences in the depth at which ash sinters and in the residence time at any given depth before final expulsion (Watkins et al. 2017; Gardner et al. 2017). An origin by in-conduit sintering explains the low porosity, the extent of open-system degassing of volatiles (Watkins et al. 2017), and trapped lithic fragments within obsidian pyroclasts (Rust et al. 2004; Gardner et al. 2017).

To explore the timescales involved in ash sintering, Gardner et al. (2018) experimentally subjected rhyolitic ash to temperatures and H_2O pressures approximating those in the conduit. They found that ash-sized particles can equilibrate their dissolved volatile contents and sinter to vesicle-poor melt in as little as a few minutes, demonstrating that dense melt can form on the timescale of an eruption and thus obsidian pyroclasts need not be pieces of quenched magma emplaced before the eruption (cf. Newman et al. 1988; Dunbar and Kyle 1992; Rust and Cashman 2007).

The experimental results of Gardner et al. (2018) validated the timescales for sintering ash to obsidian, but they did not address the vesicle textures of obsidian pyroclasts. In fact, many textures of the North Mono obsidian pyroclasts do not match those predicted by isothermal sintering. For example, sintered samples reach an equilibrium porosity of ~ 3–5 vol.% (Wadsworth et al. 2016; Gardner et al. 2018), which is thought to be the point at which permeability approaches zero, and porosity becomes isolated (Wadsworth et al. 2017). Although the value of 3 vol.% is in good agreement with predictions from percolation theory and simulations (Kertész 1981; Elam et al. 1984; Vasseur and Wadsworth 2017), the majority of obsidian pyroclasts from the North Mono eruption have ≤ 1 vol.% vesicles and some have no vesicles. Other textural variations in the natural samples include vesicles that range in shape from spherical to highly distorted and in number densities (N_v) between 0 (i.e., no vesicles) and ~ 10^8 vesicles per cm^3 (Gardner et al. 2017). Volatile contents are also heterogeneous, regardless of vesicularity, and even very vesicle-poor obsidians have sub-domains with contrasting H_2O and CO_2 contents (Watkins et al. 2017).

Many textures seen in the North Mono obsidian pyroclasts were thus not captured by the experiments presented in Gardner et al. (2018) or indeed in any other experimental work designed to probe the origin of sintered rhyolitic deposits (Wadsworth et al. 2014). To address this gap, we carried out sintering experiments that complement those of Gardner et al. (2018) but aim to replicate more accurately the natural scenario by using different particle sizes, mixed particle-size distributions, and by imposing cooling on the sintering particle pack. Combined, these results provide an improved framework in which to interpret the vesicle textures of obsidian pyroclasts.

Methods

All experiments used the same rhyolitic obsidian used by Gardner et al. (2018), the composition of which is listed in Table 1. This obsidian has a starting H_2O concentration of 0.15 wt.% (Gardner et al. 2018). The obsidian was crushed into pieces with a steel mortar and pestle, and then those pieces were ground to a powder using an agate mortar and pestle. The powders were sieved at different times during the grinding process to produce splits of different particle sizes. The first split consisted of particles that remained on the no. 35 (500 μm) and no. 60 (250 μm) mesh sieves. Because of their irregular shapes, the ash particles in this split have dimensions that are smaller and larger than 250–500 μm. We measured 20 random particles under the microscope and found that they had principal axes of 696 ± 244, 429 ± 73, and 212 ± 81 μm; we refer to this sample as “coarse ash.” The second split consisted of particles that passed through the no. 325 (45 μm) mesh sieve. Under the microscope, we found that these are ≤ 2 to 45 μm in size; we refer to this sample as “fine ash.”

Separately, a cylindrical core was drilled from the obsidian and hydrated at 875 °C and 40 MPa, following the methods of Gardner and Ketcham (2011). The resulting sample was clear rhyolitic glass with ~ 2.3 wt.% dissolved H_2O, as measured by Fourier transform infrared (FTIR) (see below). The glass was crushed, ground, and sieved, and we collected particles that remained on the no. 80 (180 μm) mesh sieve. Measurements of 20 random particles revealed that they are blockier than the coarse ash, with principal axes of 298 ± 45, 209 ± 33, and 159 ± 25 μm; we refer to this sample as “wet ash.”

Each experiment used ~ 30–40 mg of powder (Table 1). In one set of experiments, we used only one of the unimodal samples described above (fine, coarse, or wet). These experiments serve as a calibration of the sintering timescales for each population, before mixing populations. In a second set of experiments, we used bimodal mixtures consisting of the fine ash mixed with either ~ 25 or ~ 50 wt.% coarse ash or 50 wt.% wet ash.

Table 1 Experimental run conditions and results

Run[a]	P[b] (MPa)	T[b] (°C)	t[b] (min)	Fine[c] (mg)	Coarse[c] (mg)	Wet[c] (mg)	ϕ[d] (vol.%)	log N_v[e] (cm^{-3})	Size[e] (μm)
G–1766	22	750	5	31.3	0	0	45.7	n.d.	–
G–1765	22	750	10	30.1	0	0	22.3	n.d.	–
G–1728	22	750	20	31.4	0	0	4.9	7.80	2–4
G–1729	22	750	30	31.9	0	0	3.2	7.66	1–15
G–1759	22	750	47	32.2	0	0	4.7	7.53	1–38
G–1758	22	750	60	32.8	0	0	5.4	7.50	2–48
G–1769	22	750	30	0	42.1	0	n.d.	n.d.	–
G–1768	22	750	60	0	40.2	0	n.d.	n.d.	–
G–1772	22	750	30	0	0	39.7	34.6	n.d.	–
G–1773	22	750	60	0	0	41.2	31.9	n.d.	–
G–1724	22	750	20	20.2	20.5	0	32.6	n.d.	–
G–1760	22	750	45	20.4	22.0	0	25.5/3.5	7.20	n.d.
G–1762	22	750	60	19.7	20.9	0	7.6	7.34	1–20
G–1761	22	750	20	30.0	10.0	0	16.2/6.7	7.54	1–10
G–1763	22	750	45	30.6	9.3	0	7.4/5.4	7.63	1–16
G–1764	22	750	60	30.0	10.2	0	3.1	7.59	1–84
G–1767	22	750	20	15.1	0	15.5	27.9/9.0	7.75	1–20

n.d. not determined, − no spherical vesicles present

[a] Composition of obsidian used in all experiments (all oxides in wt.%, with all Fe reported as FeO: $SiO_2 = 76.53$; $TiO_2 = 0.06$; $Al_2O_3 = 13.01$; $FeO^* = 0.79$; $MnO = 0.08$; $MgO = 0.02$; $CaO = 0.74$; $Na_2O = 3.87$; $K_2O = 4.91$

[b] Pressure (in MPa), temperature (in °C), and run duration (in minutes) of the experiment

[c] Mass of "fine" (dry, ≤ 45 μm), "coarse" (dry, 250–500 μm), and wet (hydrated, 125–180 μm) powders in sample

[d] Porosity (in vol.%) of the experiment, including all vesicle types. If two values are listed, the first is porosity of matrix between closely spaced large particles and the second is the porosity of the matrix far away from large particles

[e] Number density (in numbers per cubic centimeter) of all vesicles present and range of sizes of spherical vesicles only

Each sample was weighed into a gold capsule (3 mm O.D.) that was welded shut on one end. The other end of the capsule was left open. Each capsule was placed into a sample holder at the end of an Inconel rod, which was then inserted into a pressure vessel fitted with a rapid quench extension, as described in Gardner (2007). The pressure vessel was connected to the pressure line, and 22 MPa of H_2O pressure was applied. Because the capsule was open at one end, the pressurized H_2O was in contact with the powder and thus the interstitial interconnected pore space was at the same pressure as that in the pressure vessel. The capsule thus exerted no stress on the particles within, and the only stress driving sintering arose from interfacial tension between the molten particles and interstitial H_2O (Gardner et al. 2018).

An external magnet held the sample rod in place, which held the sample inside a water-cooled jacket while the pressure vessel heated to 750 °C, as measured by K-type thermocouples precise to ± 5 °C. When the vessel thermally equilibrated, pressure was set at ~ 2.0 MPa above 22 MPa, as measured by a pressure transducer precise to ± 0.1 MPa. The external magnet was then raised, lifting the sample into the hot zone of the pressure vessel in ~ 1 s; there was an associated pressure drop of ~ 2.0 MPa. Pressure was then quickly adjusted to 22 MPa in ~ 15 s. The sample was held in place for 5 to 60 min (Table 1). During that time, pressure varied by no more than 0.1 MPa and temperature varied by no more than 1 °C. After the target time was reached, the magnet was lowered, bringing the sample into the water-cooled jacket where it cooled at ~ 100 °C per second (Gardner et al. 2018). When the sample was lowered, pressure increased by ~ 2.0 MPa but was quickly adjusted back to 22 MPa in ~ 15 s.

In a final set of experiments, samples were sintered isothermally for a given time and then cooled slowly to a specified temperature before being quenched rapidly, to investigate the effects of cooling on final textures (Table 2). In this set of experiments, most samples consisted of fine ash—one held a 50:50 mix of fine and coarse ash—that were first held at 22 MPa and 750 °C for 5, 10, or 30 min, mimicking the isothermal experiments described above; the furnace was then switched off to allow the samples to cool. The rate of cooling changed with time, because it was controlled by the heat loss from the insulated furnace: it took 49.6 ± 5.7 s to cool from 750 to 748 °C and then another 36.2 ± 3.9 s to cool to 745 °C. After that, samples cooled at an approximately constant rate of

Table 2 Cooling experiments, conditions, and results

Run	P^{a} (MPa)	T_{s}^{a} (°C)	t_{s}^{a} (min)	T_{f}^{b} (°C)	t_{f}^{b} (min)	Fine^{c} (mg)	Coarse^{c} (mg)	ϕ^{d} (vol.%)	log N_{v}^{e} (cm^{-3})	Size^{e} (μm)
G–1788	22	750	5	550	22:44.6	30.7	0	7.4	n.d.	n.d.
G–1787	22	750	10	650	12:06.6	32.3	0	10.4	n.d.	n.d.
G–1789	22	750	10	550	24:53.4	34.3	0	3.2	n.d.	n.d.
G–1786	22	750	30	700	6:10.2	29.4	0	0.9	6.83	n.d.
G–1784	22	750	30	650	11:17.3	30.3	0	0.3	5.41	15–35
G–1783	22	750	30	550	22:56.7	30.3	0	0	0*	0
G–1785	22	750	30	650	11:01.2	20.2	20.8	15.9/1.8	6.25	n.d.

n.d. not determined. N_v in G–1783 is 0 cm^{3}

[a] Pressure (in MPa) and temperature (in °C) of sintering for duration *t* (in minutes)

[b] Final temperature (in °C) of cooling and duration of cooling (in minutes) to final temperature

[c] Mass of "fine" (dry, ≤ 45 μm) and "coarse" (dry, 250–500 μm) powders in sample

[d] Porosity (in vol.%) of the experiment, including all vesicle types. If two values are listed, the first is the porosity of matrix between closely spaced large particles, and the second is porosity of matrix far away from coarse particles

[e] Number density (in numbers per cubic centimeter) and range of sizes of all vesicles present

9.4 ± 0.3 °C per minute, and the samples reached 700 °C by 6.3 ± 0.3 min, 650 °C by 11.4 ± 0.6 min, and 550 °C by 23.5 ± 1.2 min. Although cooling slowed below 650 °C, the change was not significant. Throughout cooling, pressure was maintained within 0.1 MPa of 22 MPa. All samples were quenched rapidly as soon as they reached the final target temperature.

Experiments were run over a range of temperatures from 550 to 750 °C at 22 MPa. Assuming H_2O solubility (see below), those conditions equate to dissolved H_2O contents of 1.8 to 2.2 wt.% (Liu et al. 2005). We estimate that melt viscosity was thus ~ $10^{7.1}$ to $10^{10.1}$ Pa s (Hess and Dingwell 1996), which is well below a viscosity of $10^{11.4}$ Pa s that is typically considered for the glass transition (Gottsmann et al. 2002). Therefore, under all conditions of our experiments, the samples were fluid and could behave as melts.

All samples were extracted from their gold capsules and, if coherent, sealed in epoxy and thin sectioned to about 500 μm thickness. A petrographic microscope was used to inspect sample textures and measure vesicle numbers, shapes, and sizes. Vesicle sizes were measured using a graduated ocular on the petrographic microscope and are precise to ± 0.5 μm. The number density of vesicles (N_V) was measured by selecting different areas in a sample and counting all vesicles that appear as the field of view is moved through it using the focusing knob of the microscope; N_V is thus number density per unit total volume (melt plus vesicles). The depth viewed was measured using a Heidenhain focus drive linear encoder. All vesicles, regardless of shape, were counted, but only spherical vesicles were measured for size. Porosity (ϕ) was measured by photographing samples in reflected light and then using NIH *ImageJ* to make binary images of the photographs to measure pore areas relative to the entire area of the image and converted directly to porosity (vol.%). Errors on ϕ are estimated at 10% of the measured value.

Glasses in the hydrated core, G–1724, G–1728, and G–1762 (Table 1), were analyzed for dissolved H_2O contents by FTIR spectroscopy in transmittance mode, using a Thermo Electron Nicolet 6700 spectrometer and Continuμm IR microscope. Spectra were collected using 60 scans at a resolution of 4 cm^{-1} and measured either in near-IR (7000 to 3800 cm^{-1}) with white light and a CaF_2 beamsplitter or in mid-IR (4000 to 650 cm^{-1}) with a globar source and KBr beamsplitter. Dissolved contents of molecular water (H_2O_m) and hydroxl water (OH) were determined from absorbances at ~ 5250 and ~ 4500 cm^{-1}, respectively, using the model of Zhang et al. (1997), or from the broad absorbance at ~ 3500 cm^{-1}, using an absorptivity of 75 L mol^{-1} cm^{-1} (Okumura et al. 2003). Sample thickness where each spectrum was collected was determined using the method described above.

Area maps of OH, H_2O_m, and total H_2O concentrations were made for G–1783 (Table 2) using a Thermo Nicolet Nexus 670 FTIR spectrometer, following the methods of Watkins et al. (2017). All measurements were made using a 15× objective, an infrared source, an MCT-A detector, and a KBr beamsplitter. Absorbances were converted to concentrations using the model of Zhang et al. (1997). The thickness of the sample was measured in several spots using a digital caliper with 0.001 mm precision. All spectra were collected at a resolution of 4 cm^{-1}, 64 scans per spot, and 64 scans for the background, which was collected every 10 min. Two maps were made, one using a 100-μm × 100-μm aperture and step size of 100 μm and the other a 40-μm × 40-μm aperture and a step size of 40 μm. No significant differences were detected between the two maps.

Experimental results

Experiments using unimodal powders

Post-experimental samples of sintered fine ash were all sufficiently coherent to section and analyze (Table 1). The highest measured porosity was ~46 vol.% for a sample that was incipiently sintered, which suggests that initial, unsintered porosity was slightly higher. This is consistent with the initial porosities measured by Gardner et al. (2018), who found that ash poured into capsules has an initial porosity between the particles of 45 and 55 vol.%, with less polydisperse ash having higher porosity. Over run durations from 5 to 60 min, porosity decreased to the apparent equilibrium of ~3–5 vol.%, which was reached after 20 min (Fig. 1). After 20 min, the sample of sintered fine ash (G–1728) has 1.77 ± 0.20 wt.% H_2O dissolved in the glass, which agrees well with the H_2O content (1.81 wt.%) predicted by the model of Liu et al. (2005). Gardner et al. (2018) also found that dry ash fully saturated within 20 min at 750 °C and 40 MPa.

After 5 and 10 min, samples of sintered fine ash consist of completely open and connected pore space around individual ash particles that are still visible, although their edges have sintered to their closest neighbors, forming arcuate necks (Fig. 2a). After 20 min, most pores are isolated from neighbors, but about two thirds of these vesicles are still distorted; the other third are spherical (Fig. 2b, c). Between 30 and 60 min, the proportion of distorted vesicles decreases significantly (Fig. 2d), and by 60 min, essentially all are spherical (Fig. 2e). By 20 min, spherical vesicles are < 2–5 μm in diameter but, later, larger ones become abundant. The larger vesicles did not grow from smaller ones but instead result from large contorted vesicles taking longer to relax in shape. Values for N_V are ~$10^{7.5–7.8}$ cm^{-3} (Table 1).

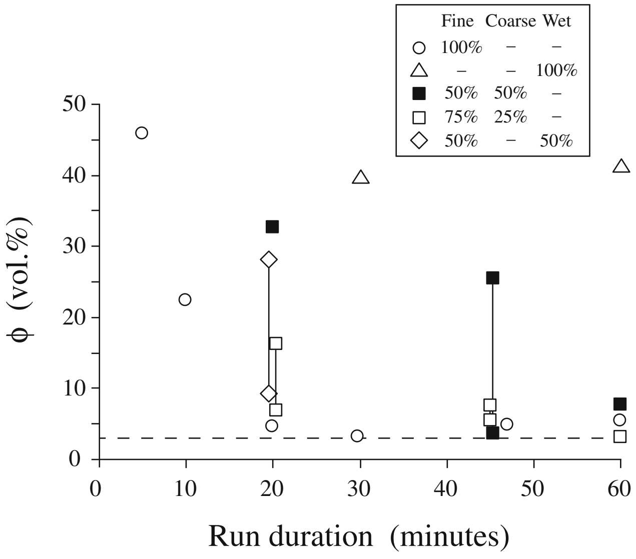

Fig. 1 Sample porosity (ϕ, in vol.%) as a function of experimental sintering time. High and low porosities of heterogenous samples are linked by vertical tie lines. All porosities are precise to ±10%. Experiments of coarse ash only ran for 30 and 60 min but did not sinter. The equilibrium porosity of $\phi = 3$ vol.% is shown as a dashed line (Wadsworth et al. 2016; Gardner et al. 2018)

Gardner et al. (2018) proposed a classification for the textural evolution of sintering unimodal rhyolitic ash, which identifies four phases: (1) particles are loose and lack cohesion; (2) particles are sintered at their contacts but are interpenetrated in a continuous, tortuous pore space; (3) porosity is no longer fully connected, with small isolated spherical vesicles and networks of larger vesicles that remain multicuspate in shape; and (4) dense glass with fully isolated, spherical vesicles and maybe a few larger complex-shaped ones; duration of each phase depends strongly on melt viscosity. We use this framework to present the results of these experiments with unimodal samples, finding that the textures of the sintered fine ash follow the same progression (Fig. 3). Samples sintered for 5 and 10 min consist of individual particles partially sintered in open pore space (Phase 2). Between 20 and 45 min, samples have low porosities, but distorted vesicles make up 40 to 70% of the population (Phase 3). After sintering for 60 min, the sample consists of dense glass with only spherical vesicles (Phase 4).

The two experiments using only coarse ash were run for 30 and 60 min but remained unsintered and crumbled to loose powder on extraction from the capsules, implying that the interparticle porosity did not decrease much below the initial value and the samples remained in Phase 1. The two experiments using only wet ash were coherent enough to section, and both consist of individual ash particles that are only slightly sintered along their edges (Fig. 2f). The particles are dispersed among an open and connected pore space that makes up 30–35 vol.% of the samples (Fig. 1). The wet ash samples thus remained in Phase 2 of textural evolution even after 60 min.

Experiments using bimodal mixed ash populations

In all mixed ash samples, even when sintering has progressed significantly—which normally removes evidence of individual particles—the coarse or wet ash component can still be recognized as large non-vesicular domains and in the case of wet ash as microlite-free domains. Overall, bimodal samples sinter more slowly, as measured by the evolution of porosity, than samples that consisted of only fine ash (Fig. 1).

In describing the final textures of the mixed ash samples, we use *matrix* to refer to domains that initially consisted of fine ash between areas that were initially either coarse or wet

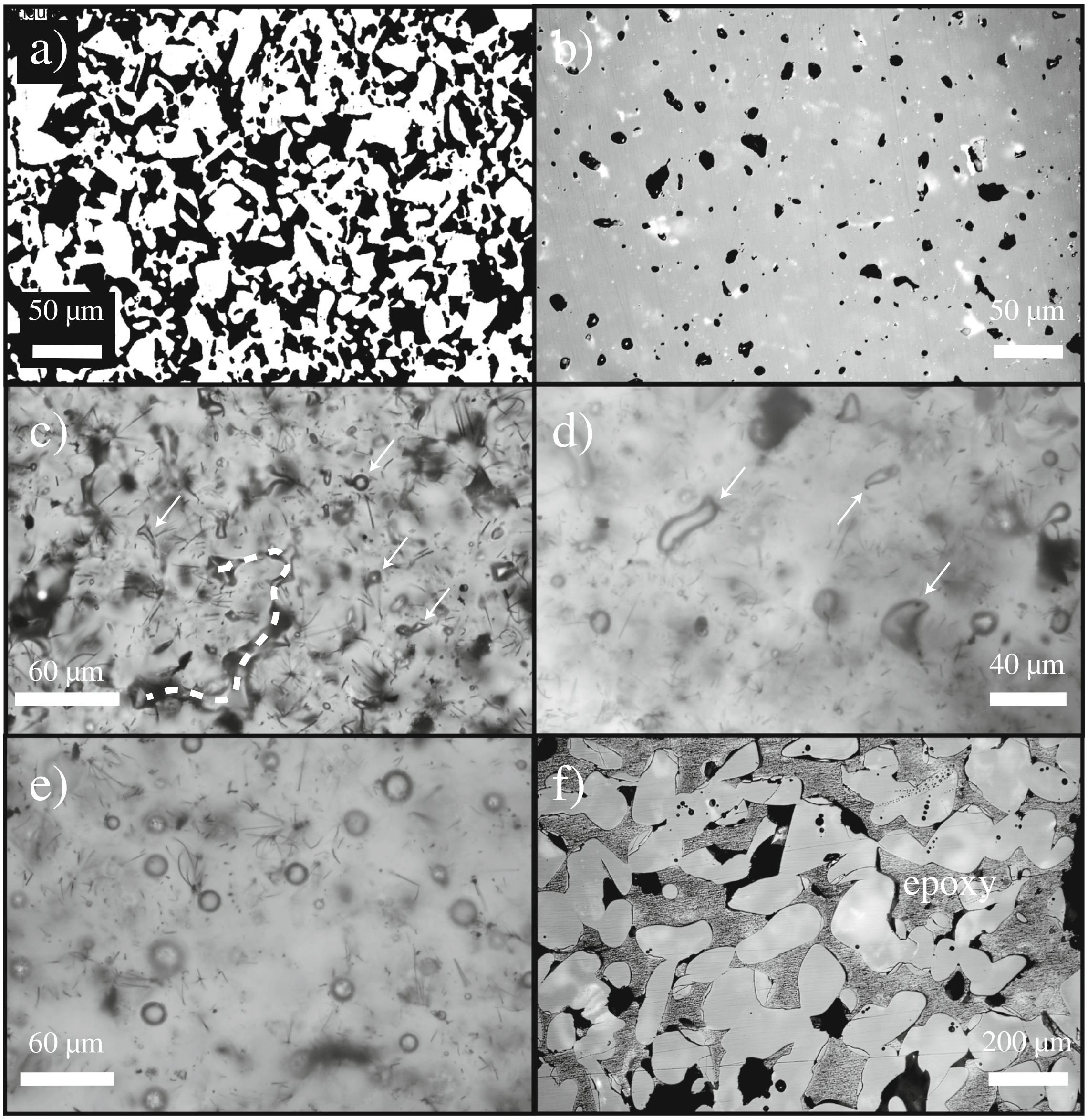

Fig. 2 Photomicrographs of sintered unimodal ash. **a** Binary threshold image of G–1766 (fine ash, $t = 5$ min) with incipiently sintered particles (white) dispersed in a continuous porous network (black). **b** Reflected light image of G–1728 (fine ash, $t = 20$ min) with dense glass and dispersed, contorted vesicles (in black). **c** Transmitted light image of the same sample in **b** with isolated spherical (arrows) and highly contorted vesicles. Dashed line traces one chain of connected vesicles. **d** Transmitted light image of G–1759 (fine ash, $t = 47$ min) with isolated, contorted vesicles (arrows). **e** Transmitted light image of G–1758 (fine ash, $t = 60$ min) with only spherical vesicles. **f** Reflected light image of G–1772 (wet ash, $t = 30$ min) with incipiently sintered particles dispersed in a continuous porous network, now mainly filled with epoxy

particles. When coarse ash makes up half of the sample, the matrix after 20 min (G–1724) consists of small ash particles that are slightly sintered surrounded by ~ 33 vol.% of pore space (Fig. 4a). Pockets of large vesicles occur in the matrix that can be ≥ 800 µm in size, with most pockets found in the vicinity of relict large particles. FTIR measurements show that the large relicts have 0.57–1.79 wt.% H_2O dissolved in them (measured in the interiors of large particles, as far away from the edges as possible), which is below the solubility value of 1.81 wt.% (Liu et al. 2005). After 45 min, matrix porosity is still heterogeneous and depends on proximity to relict coarse particles (Fig. 4b, c). Where coarse particles are closer together than ~ 200 µm, the matrix is of the order of 26 vol.% porous and can preserve pockets of large vesicles up to 600 µm long; where farther apart, the matrix is only about 4 vol.% porous. In both regions, $N_V \sim 10^{7.2}$ cm^{-3} and the vast majority of vesicles are distorted and connected together via narrow channels. After 60 min, the matrix is almost uniformly dense, and

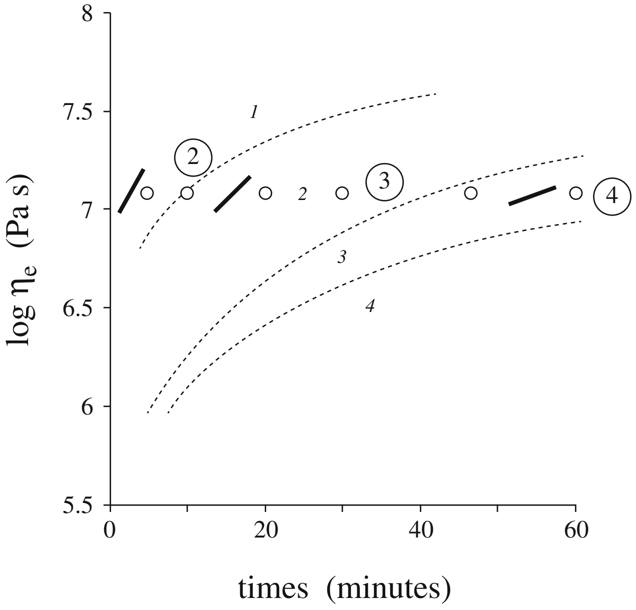

Fig. 3 Sintering textures of fine ash samples (open circles) as a function of equilibrium melt viscosity (η_e, in log Pa s) and experimental time. Solid lines demark approximate phases of constant texture. In Phase 1, individual particles remain loose and lack cohesion. In Phase 2, particles are sintered only at their contacts and porosity is fully open. In Phase 3, particles are merged together and vesicles are nearly sealed, but many vesicles are still multi-cuspate shaped. In Phase 4, samples are dense glass with isolated vesicles. Dashed curves (with small numbers) are for coarser ash sintered in Gardner et al. (2018)

large pockets of vesicles are rarer and ≤ 200 μm in size (Fig. 4d). All vesicles are isolated, but only about half are spherical. The dissolved H_2O contents in the interiors of the relict coarse particles are 1.84 (± 0.14) wt.%, which is within error of the 1.81 wt.% saturation limit of H_2O (Liu et al. 2005).

A similar progression of textures is observed when coarse ash makes up only ~ 25 wt.% of the sample, except that matrix porosity is lower after any given amount of time (Fig. 1). Relatively large porous pockets still exist, but they are generally smaller and few remain after 45 min. One experiment that contained fine ash and 50 wt.% wet ash was run for 20 min. Its matrix is similar in porosity to that of the coarse ash mix that sintered for more than twice as long (Fig. 1). It contains large pockets of vesicles up to 300 μm long and mainly highly contorted, multi-cuspate vesicles; only about 16% of the vesicles are spherical.

Overall, the temporal evolution of textures in the mixed ash populations is broadly similar to the unimodal case for fine ash, such that porosity generally decreases with time and the end-state is isolated vesicles (Fig. 1). The presence of large particles, however, slows the rate of decrease in porosity and causes individual vesicles to take longer to relax to spherical. After 60 min, for example, 13–20% of the matrix vesicles are still distorted in samples with 50% coarse particles, whereas all were spherical in samples of fine ash only. Another important difference is that bimodal samples produce textures that are considerably more heterogeneous, with pockets of large vesicles. These pockets generally decrease in size with time and are less abundant when coarse particles are less abundant.

Experiments combining sintering and cooling

Six samples of fine ash were cooled slowly after sintering at 750 °C (Table 2). All have significantly reduced porosities compared to samples that were not slowly cooled (Fig. 5). For example, sintering isothermally for 5 min produced only incipiently sintered particles among ~ 45 vol.% connected pore space, whereas subsequent cooling to 550 °C produced dense glass with 7 vol.% isolated vesicles. Importantly, cooling is found to be able to produce dense glass with no measurable vesicles (Fig. 5) and reduced N_v from $10^{7.66}$ cm^{-3} to zero vesicles (Table 2). FTIR mapping across G–1783 (no vesicles present) found H_2O concentrations between 1.88 and 2.16 wt.%, averaging 2.03 ± 0.06 wt.%. That range falls between solubility H_2O concentrations expected at 750 to 550 °C and 22 MPa (Liu et al. 2005).

Although porosity is reduced during cooling, the preserved vesicles are relatively more deformed than those found after similar durations at high temperature. For example, after 30 min of sintering at 750 °C (G–1729), about half of the vesicles have relaxed to spherical shape (Fig. 6a). In contrast, G–1789, which sintered for 10 min at 750 °C and then cooled to 550 °C for ~ 25 min (total time = 35 min), has the same porosity, but all of the vesicles are distorted in shape (Fig. 6b). Cooling can thus prolong the time it takes for distorted vesicles to relax to spherical, while simultaneously reducing overall porosity.

One sample that consisted of equal proportions of fine and coarse ash was cooled to 650 °C after sintering for 30 min (G–1785; Table 2). Given the total amount of time spent at elevated temperature (41 min), this sample would be expected to have a porosity of ~ 3 vol.% far from large particles and ~ 26 vol.% near relict particles (compared to G–1760; Table 1). Instead, the corresponding values for the cooled sample are ~ 2 and ~ 16 vol.%. Furthermore, cooling reduced N_V by an order of magnitude compared with the isothermal sample (Tables 1 and 2).

Analysis of experimental results

The textural descriptions above highlight some of the complexities of the sintering process for rhyolitic particles that have not been accounted for in existing sintering models

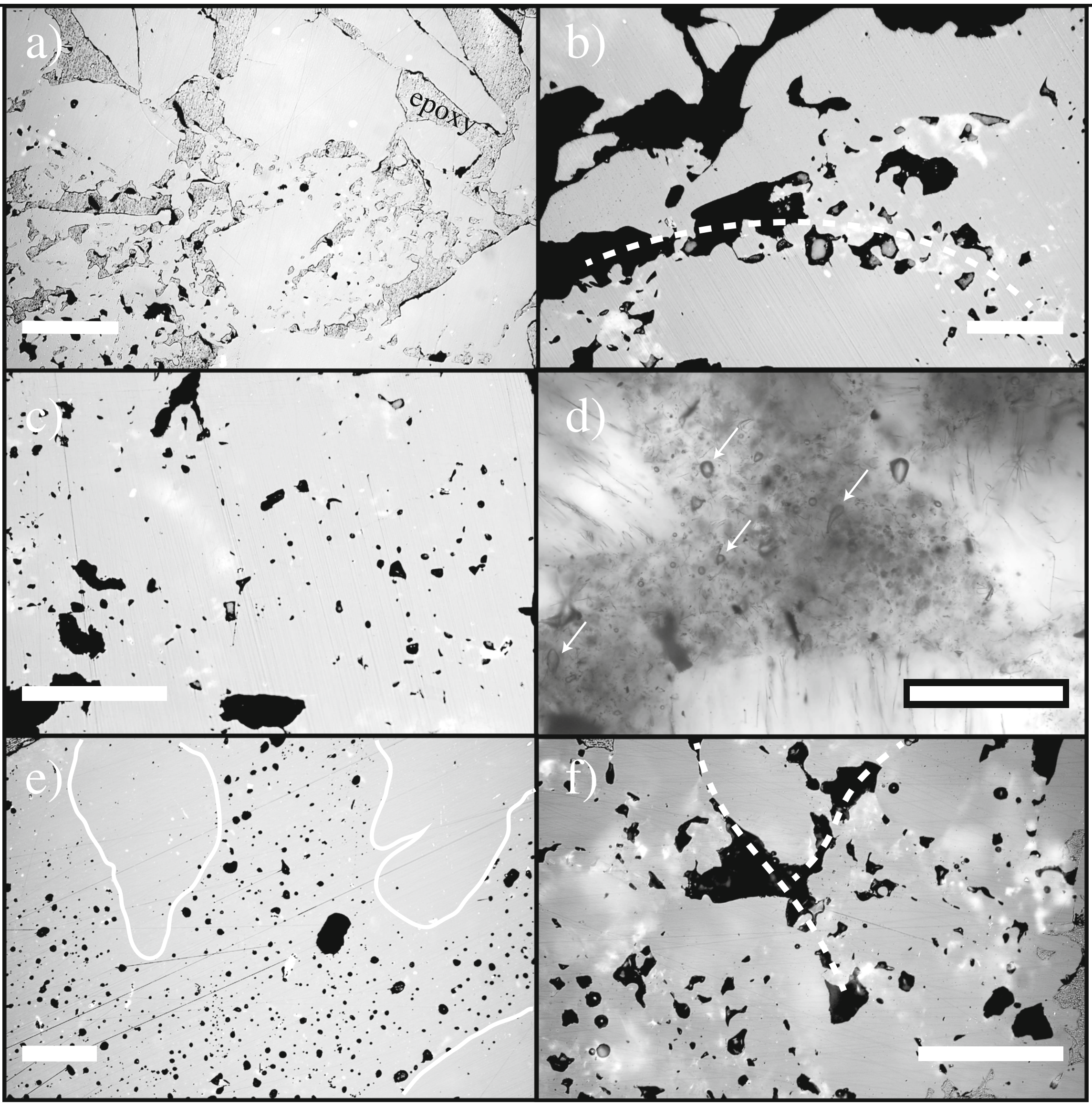

Fig. 4 Photomicrographs of sintered bimodal samples (all scale bars are 200 μm long). **a** Reflected light image of G–1724 (50:50 fine/coarse ash, $t = 20$ min) with incipiently sintered particles in a continuous porous network, now mainly filled with epoxy. **b** Reflected light image of G–1760 (50:50 fine/coarse ash, $t = 45$ min) with highly porous matrix between closely spaced large particles; dashed line traces a large continuous pocket of large vesicles > 1 mm long. **c** Reflected light image of same sample as **b** but with low porosity matrix where large particles are far apart. **d** Transmitted light image of G–1762 (50:50 fine/coarse ash, $t = 60$ min) with homogeneous matrix with spherical vesicles (arrows) between large relict particles. **e** Reflected light image of G–1763 (75:25 fine/coarse ash $t = 45$ min) with homogeneous porous matrix among large particles (outlined in white). Large vesicle in the middle is part of a longer pocket ~ 300 μm long. **f** Reflected light image of G–1767 (50:50 fine/wet ash, $t = 20$ min) with highly porous matrix between closely spaced large particles; dashed lines trace continuous pockets of large vesicles

(Wadsworth et al. 2014, 2016). Here, we place these experiments in the context of existing theoretical constraints to highlight these differences.

Gardner et al. (2018) defined two timescales relevant to sintering of unimodal rhyolite particles that were also hydrating. The first timescale is for diffusive hydration (λ_d), during which the dissolved H_2O content increases from the initial value of 0.15 wt.% to the saturation value, which depends on the sintering temperature and pressure. The second timescale is for sintering (λ_s). For randomly packed, monodisperse spherical particles (droplets when molten), the sintering timescale is given by

$$\lambda_s = \frac{\eta L}{\sigma} \tag{1}$$

where η is droplet viscosity (Pa s), σ is surface tension (N m^{-1}), and L (m) is a characteristic length scale, which can be approximated as the mean particle radius ($\overline{R}$) in the

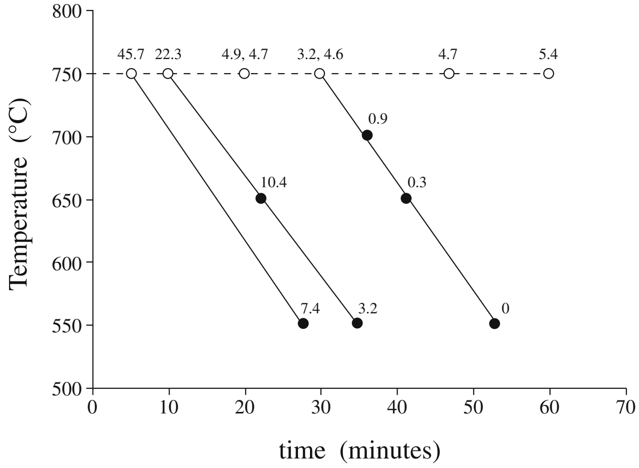

Fig. 5 Temperature versus total run duration for fine ash samples that were either sintered at 750 °C (open circles) or sintered at 750 °C and then cooled (solid circles). Final porosity (vol.%) values are listed next to each sample. Note that samples plot along nearly linear cooling lines (solid curves), showing that cooling occurred at a relatively steady rate

case of sintering angular particles (Gardner et al. 2018). The diffusive hydration timescale is given by

$$\lambda_d = \frac{\overline{R}^2}{D} \tag{2}$$

where D is the diffusivity of H_2O in rhyolite. Both η and D are material properties that must be computed from constitutive models. We use the model of Hess and Dingwell (1996) to compute η as a function of dissolved H_2O concentration (C) and temperature (T). In turn, we use the model of Liu et al. (2005) to compute C at isothermal temperature (T_0) and isobaric pressure (P_0). We use the model of Zhang and Ni (2010) to compute D, as a function of C, T_0, and P_0. We set $\sigma = 0.22$ N m^{-1}, following Gardner et al. (2018) for the same starting material.

Comparing timescales yields the dimensionless capillary Peclet number $(P_c) = {}^{\lambda_d}/_{\lambda_s}$ (Gardner et al. 2018). For $\lambda_d \ll \lambda_s$ (i.e., $P_c \ll 1$), diffusive hydration occurs rapidly compared with sintering. Conversely, for $\lambda_d \gg \lambda_s$ (i.e., $P_c \gg 1$), sintering occurs rapidly compared with diffusive hydration. Because both timescales depend on C, and C changes over time during the experiments, we need to establish what value of C to use to compute the timescales. We assume that the particles have equilibrium H_2O concentrations (C_e) for $P_c \ll 1$, and the particles have their initial H_2O concentrations for $P_c \gg 1$. Gardner et al. (2018) found that sintering can be assumed to be proceeding at equilibrium conditions as long as $P_c \lesssim 10$ (the low-Pc regime). All unimodal experiments of this study meet the condition $P_c < 10$, implying that hydration was complete before sintering. This is confirmed by measurements of H_2O concentration in G–1728 (measured for experimental conditions where time $>\lambda_d$), which is within uncertainty of C_e. We thus assume C_e has been reached and use that value to compute the viscosity at C_e (which we term η_e) in (1) to predict λ_s.

The metric most commonly used to track the progression of sintering is the interstitial porosity (ϕ) to the particles (Wadsworth et al. 2014, 2016). Wadsworth et al. (2016) found an analytical approximation of a full sintering model that can be used to predict the porosity of a random pack of particles as a function of time (t) following

$$\phi(t) = \phi_i \exp\left(-\frac{3t}{2\lambda_s}\right). \tag{3}$$

This expression has been validated for angular particles (Gardner et al. 2018; Wadsworth et al. 2014). We find that the predicted $\phi(t)$ curve computed using (3), with λ_s computed from (1), agrees well with the unimodal data using very different ash sizes as starting materials (Fig. 7). Note, initial porosity is taken as $\phi_i = 45$ or 60 vol.%, and there are no adjustable parameters.

In the case of bimodal experiments, which contained two different $\overline{R}$ values in different proportions, the sintering process is complicated because the values of λ_d are different for each constituent particle size class in the mixed population. This means that there can be conditions for which $t < \lambda_d$ for large particles while $t > \lambda_d$ for small particles. This is illustrated by the cores of coarse particles in G–1724 having measured H_2O concentrations that is just over half of C_e, whereas, after the same amount of time, unimodal fine ash in G–1728 is fully hydrated. The result of this is that a system can be sintering particles with very different viscosities. Despite such complexities, we found that the porosity of any bimodal mixture is intermediate, although heterogeneous, between predicted values for $\phi(t)$ of the end-member unimodal $\overline{R}$ classes (Fig. 7). In addition, the bimodal experiments that contain proportionally more fine ash sintered faster and hence approached the equilibrium porosity faster. While a full predictive model for bimodal (and polymodal) sintering is beyond the scope of this study, we suggest that $\phi(t)$ for bimodal sintering populations can be qualitatively estimated from those of the end-member populations.

Resorption of isolated vesicles during cooling

Assuming that the cooled samples and isothermal samples initially had similar textures before the start of the cooling ramp, our experiments demonstrate that slow cooling causes vesicles to shrink and disappear (Fig. 8). We hypothesize that this is caused by thermally driven resorption of H_2O, i.e., the increase in H_2O solubility with decreasing T is sufficient to cause all H_2O in the bubbles to resorb into the surrounding melt. McIntosh et al. (2014) first proposed that this mechanism could play a role in the formation of dense obsidian.

For bubbles to resorb completely, there must be sufficient time for all H_2O molecules within the bubbles to diffuse into the surrounding melt. There must also be enough time for the melt to flow viscously to allow the bubbles to shrink. To determine whether this is feasible in the experiments, we compare three timescales: (1) the time available for diffusion and flow, λ_a; (2) the time that would be required for H_2O to resorb diffusively, λ_γ; and (3) the time that would be required for the melt to flow, λ_η. To test the resorption hypothesis, we determine these three timescales for sample G–1783 (Table 2).

For this analysis, the time available for the bubble to resorb, λ_a, is taken simply as the duration of the cooling ramp. We derive order-of-magnitude estimates for the time required for diffusion, λ_γ, and viscous flow, λ_η, in Appendix 1. We find that the time required for diffusion to resorb all of the water in the bubbles depends strongly on the initial size of the bubble, while the time required for viscous flow to allow the bubble to collapse depends only weakly on the initial bubble size. In Fig. 8, λ_γ and λ_η are plotted (solid and dash line, respectively) as functions of initial bubble radius, given $P_o = 22$ MPa and $T_o = 750$ °C. The time available for diffusion and flow (λ_a) is also plotted for both the cooling ramp (red line) and for rapid quench (blue line). We find that, over the range of initial bubble sizes in our experiments (indicated by the gray box), the time available for resorption during slow cooling is longer than the diffusion and flow timescales, hence there is sufficient time for resorption to go to completion. In contrast, the time available for resorption during rapid cooling is shorter than both the diffusion and flow timescales; hence, there is insufficient time for resorption. This supports our hypothesis that thermally driven resorption is sufficient to cause the complete removal of the bubbles during slow cooling (Fig. 5).

To first order, therefore, we find that slow cooling of porous rhyolitic melt can cause H_2O pores to resorb and

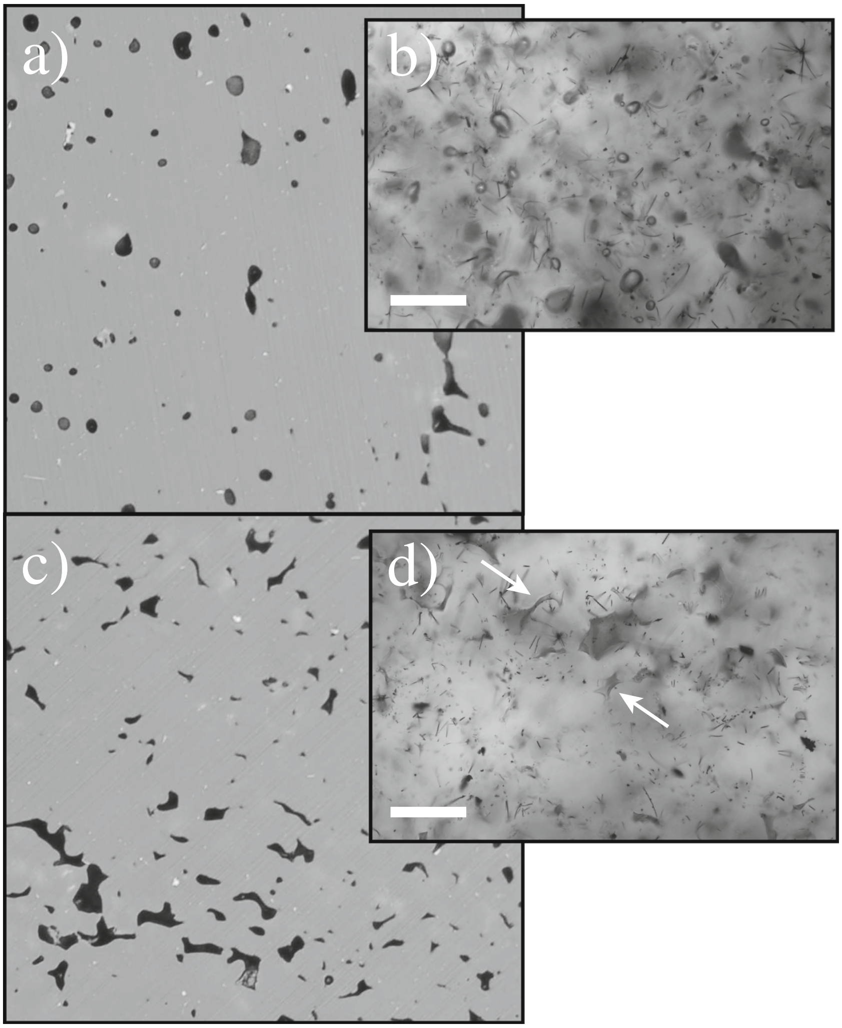

Fig. 6 **a** Reflected and **b** transmitted light images of G–1729 that sintered for 30 min at 750 °C and then quenched. **c** Reflected and **d** transmitted light images of G–1789 that sintered for 10 min at 750 °C and then cooled to 550 °C, over 25 min. Both have ~3 vol.% vesicles, but all are distorted in G–1789 (some marked by arrows), whereas half are spherical in G–1729. Images **a** and **c** are 400 μm × 400 μm; scale bars in **b** and **d** are 50 μm long

produce porosities lower than the equilibrium sintering value of 3–5 vol.%. We note, however, that our approach (Appendix 1) to determine order-of-magnitude values for λ_γ and λ_η is highly simplified. We thus caution against using this approach to make quantitative predictions about the conditions under which resorption may occur in natural systems. While such predictions are possible, it would require a numerical approach that is beyond the scope of this work.

Discussion

Our sintering experiments, combined with those of Gardner et al. (2018), place constraints on the formation of vesicle textures generated during sintering. Comparing those results to textures of natural obsidian pyroclasts provides a framework for understanding how the pyroclasts form. All experiments show that, as ash sinters, the volume of open pore space decreases and is sealed off, generating isolated vesicles (Fig. 3). Those vesicles start off highly distorted and convolute but eventually relax to spherical shapes (Fig. 2). That sequence occurs in the different sets of experiments, but the timescales for sintering and vesicle relaxation depend strongly on viscosity and initial particle size (Wadsworth et al. 2014; Gardner et al. 2018; this study). The general progression from distorted to spherical shapes observed in the experiments supports the overall premise of the model proposed by Gardner et al. (2017) for the formation of obsidian pyroclasts in the North Mono eruption. They suggested that the main mechanism for the formation of these pyroclasts is sintering of volcanic ash in the conduit, speculating that vesicles start out distorted in shape but relax to spherical with time. Furthermore, the experiments demonstrate that distorted and spherical vesicles may coexist (i.e., Phases 2–3) during the sintering process, as observed in North Mono obsidian pyroclasts (Fig. 9a).

Our experiments show that sintering unimodal ash evolves texturally towards homogeneously distributed spherical vesicles (Fig. 2e). About 10–15% of the North Mono obsidian pyroclasts studied by Gardner et al. (2017) contain only spherical vesicles (Fig. 9b; see also Fig. 5a in Gardner et al. 2017). We infer that those obsidian pyroclasts preserve the end products of sintering unimodal distributions of ash. Experimental sintering of unimodal ash also shows that N_v is related to the size distribution of particles sintered. Sintering of fine ash (≤ 45 μm; this study) produced $N_v = 10^{7.51 \pm 0.19}$ cm^{-3} (Table 1). Sintering of ash that ranged in size by 1–1600 μm ($\overline{R}$ = 89 μm) resulted in $N_v = 10^{6.55 \pm 0.23}$ cm^{-3} (Gardner et al. 2018). Sintering of coarser but less polydispersive ash of ~ 63–400 μm in size ($\overline{R}$ = 185 μm) produced even fewer vesicles, $N_v = 10^{5.62 \pm 0.19}$ cm^{-3} (Gardner et al. 2018). The differences in N_v are significant, representing one to two orders of magnitude variation in numbers of vesicles within a given volume. Vesicles in North Mono obsidian pyroclasts occur in N_v values from 0 (no vesicles) to $10^{8.1}$ cm^{-3}, but more than half have $N_v > 10^{6.8}$ cm^{-3} (Gardner et al. 2017).

We propose that North Mono obsidian pyroclasts with abundant vesicles formed by sintering fine-grained ash. Fine-grained

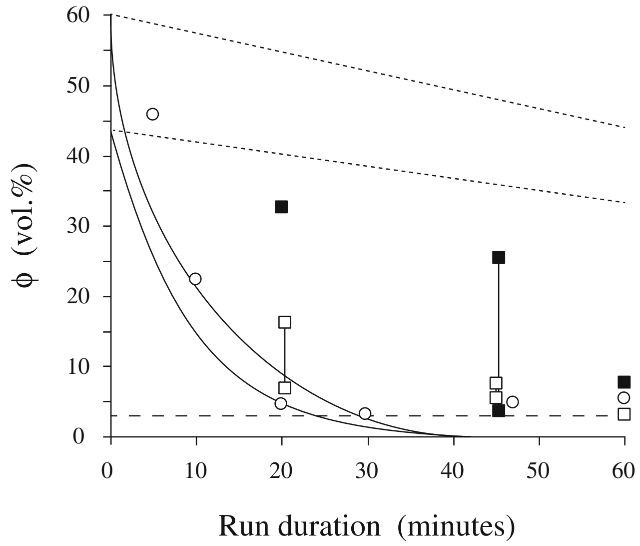

Fig. 7 Porosity (ϕ, vol.%) as a function of sintering time for samples that started with dry ash; symbols are the same as in Fig. 1; porosities are precise to ± 10%. Curves for solutions of Eq. 3 for low-Pc sintering are shown for unimodal fine ash (solid lines) and unimodal coarse ash (dashed lines), assuming $\phi_i = 45$ or 60 vol.%. All mixed fine coarse bimodal samples fall between the end-member cases. The equilibrium porosity of $\phi = 3$ vol.% is given as a limiting value (Wadsworth et al. 2016; Gardner et al. 2018)

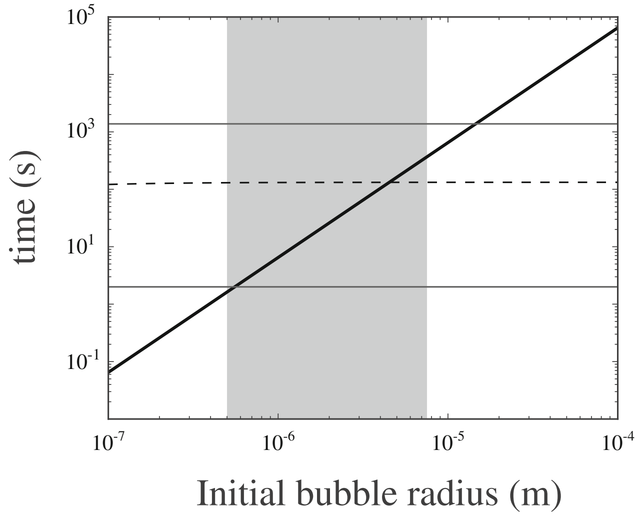

Fig. 8 Estimated duration of cooling step (over interval 750–550 °C) required to resorb bubbles of different initial size. Calculations (Appendix 1) are based on simple scaling arguments and are indicative only. Solid black line is the cooling time required to diffusively resorb all H_2O within a bubble; dashed black line is the characteristic timescale of viscous shrinkage of the bubble. Solid red line is the cooling time to 550 °C for experimental run G–1783; solid blue line is the cooling time to 550 °C for experimental run G–1729 (during rapid quench); gray box indicates range of initial bubble sizes expected in that sample. See main text for details

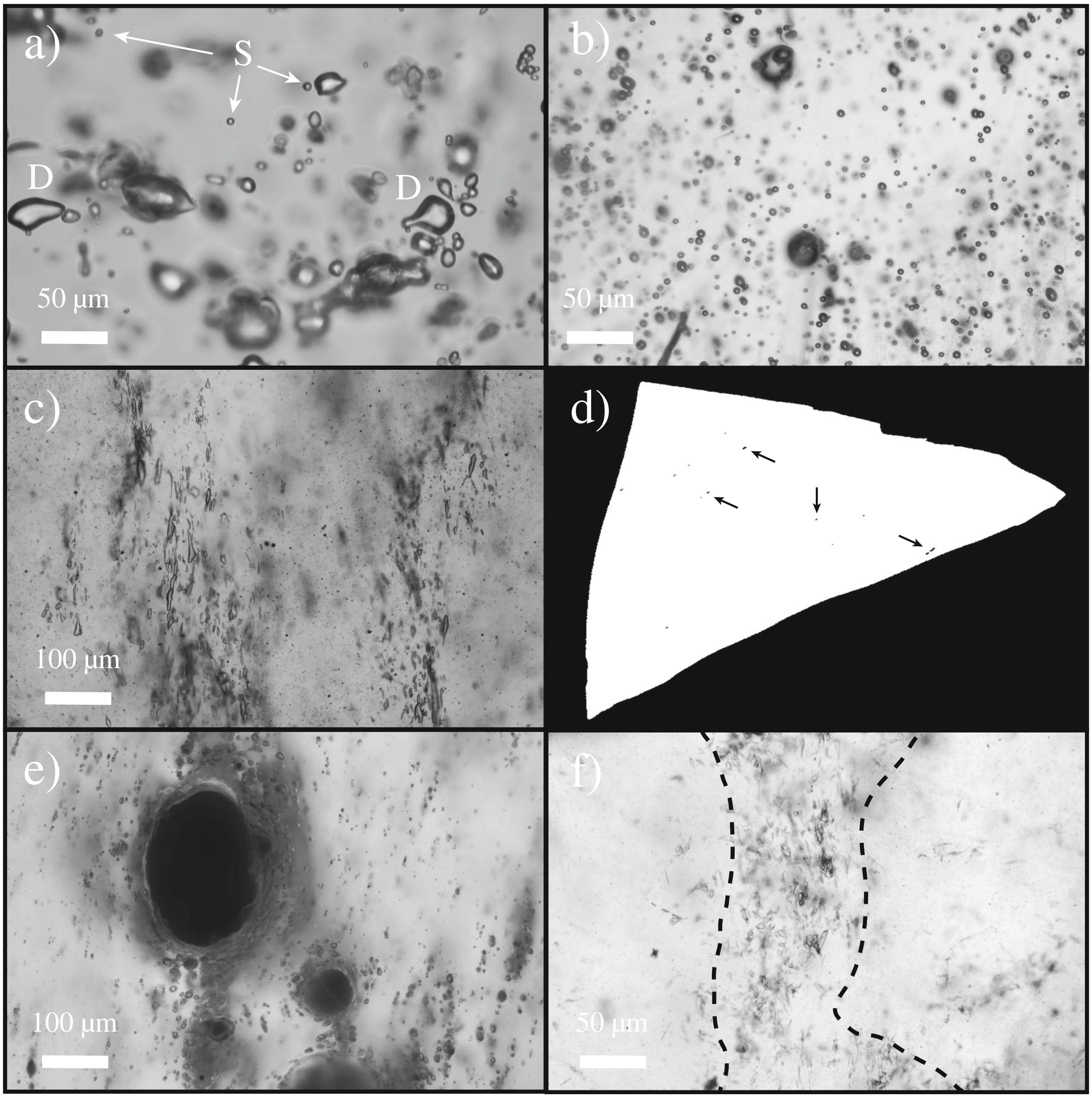

Fig. 9 Representative photomicrographs of North Mono obsidian pyroclasts (scale bars shown). **a** Transmitted light image of sample P4B–I with coexisting spherical (S) and distorted (D) vesicles. **b** Transmitted light image of sample P2–F with uniform distribution of spherical vesicles. **c** Transmitted light image of sample P10–E with bands of highly distorted vesicles. **d** Binary image of slice from High Resolution X-Ray Computed Tomography (HRXCT) scan of P10–E (same as in **c**) showing that vesicles (some marked by arrows) make up 0.04 ± 0.004 vol.% of the obsidian. Widest length of sample is ~3 mm; see supplemental materials from Gardner et al. (2017) for scanning methods. **e** Transmitted light image of sample P4B–C with large pockets of vesicles dispersed in relatively dense glass with few vesicles. **f** Transmitted light image of sample P10–I that consists of bands of glass with numerous distorted vesicles (within the dashed lines) and regions of dense glass with very few vesicles. Watkins et al. (2017) found that vesicle-poor regions in P10–I tend to be rich in H_2O, whereas the bands with abundant vesicles are rich in CO_2

ash in fact makes up a large fraction of tephra produced in explosive eruptions (Walker 1981; Kaminski and Jaupart 1998; Bonadonna and Houghton 2005; Alfano et al. 2016). If the fine ash is approximately unimodal, we show that $\phi(t)$ can be predicted, and Gardner et al. (2018) provide a full framework for estimating it at conduit conditions.

The majority of North Mono obsidian pyroclasts have < 1 vol.% porosity; furthermore, 3 of 81 samples reported by Gardner et al. (2017) were entirely vesicle-free. Experimental sintering of unimodal ash, in contrast, typically produces an equilibrium texture of 3–5 vol.% vesicles (Fig. 1; Wadsworth et al. 2014; Gardner et al. 2018). The cause of this discrepancy has remained enigmatic until now. Our experiments suggest that the relatively low porosities of the natural obsidians result from resorption induced by cooling during sintering and the associated increase in H_2O solubility in the melt (Fig. 8). We posit that many of the North Mono obsidian pyroclasts thus preserve a record of cooling during sintering. In support of this, our results show that non-spherical vesicle shapes can be preserved during cooling and may remain abundant well below the equilibrium porosity of 3–

5 vol.% (Fig. 6). Very poorly vesicular North Mono obsidian pyroclasts, in fact, contain vesicles of all shapes, including highly distorted ones (Fig. 9c, d). Only a small minority of North Mono obsidian pyroclasts are free of vesicles, which suggests that the time available for cooling was relatively short. Indeed, the overall timescale for formation of obsidian pyroclasts as deduced from diffusion modeling of volatile gradients is less than a few hours (Watkins et al. 2017).

It thus appears that some vesicle textures in natural obsidian pyroclasts can be explained by sintering of unimodal ash and that variations in textures among such pyroclasts are the result of variations in starting particle sizes and in the cooling rate. There are other textural features common to obsidian pyroclasts that are not replicated by experimental sintering of unimodal ash, such as significant spatial heterogeneities in vesicles and volatile contents within a single pyroclast (Rust et al. 2004; Rust and Cashman 2007; Castro et al. 2014; Watkins et al. 2017; Gardner et al. 2017). These include large pockets of vesicles dispersed among poorly vesicular, dense glass (Fig. 9d) and regions of poorly vesicular glass separated by glass with numerous vesicles (Fig. 9c–f). Many of these vesicular heterogeneities coincide with heterogeneous dissolved volatile concentrations (Watkins et al. 2017).

We suggest that the spatial heterogeneities in vesicles and volatiles within obsidian pyroclasts result from sintering of particles of differing size, based on our results of sintering of mixed ash populations. We found that large scale heterogeneities in vesicles can occur when samples consist of mixed ash particles (Fig. 4). For example, sintering of coarse and fine ash produced regions poor in vesicles (large relict particles) separated by porous bands of matrix (Fig. 4e). Sintering of mixed ash samples also resulted in sub-domains of matrix with large pockets of vesicles (Fig. 4b, f), which are reminiscent of isolated clusters of large vesicles in the natural obsidian pyroclasts (Fig. 9e).

The degree of heterogeneity is likely related to the contrast in sizes between sintering particles. In this study, bimodal populations resulted in highly vesicular bands separating relatively large, non-vesicular regions (Fig. 4c, e). When the sintering pack includes a wide range of particle sizes, then heterogeneities in vesicular textures range in size reflecting the particle sizes (Gardner et al. 2018). Our results additionally suggest that heterogeneities in volatile contents will result when the residence time at a given T and P is sufficient to homogenize small particles ($t < \lambda_d$) but not sufficient to homogenize large ones ($t > \lambda_d$). Commonly, the large, poorly vesicular domains in the North Mono obsidian pyroclasts are H_2O-rich relative to the vesicular domains (Watkins et al. 2017). We suggest that they are pieces of glass formed by sintering and cooling of ash that was then ripped off of the conduit walls, only to be re-plastered onto the walls and sinter with adjoining ash.

Finally, a prominent texture of North Mono obsidian pyroclasts not replicated in any sintering experiment so far is stretched/elongated vesicles (see Figs. 5c, d and 6d, f in Gardner et al. 2017). Such stretched vesicles usually align with their neighbors, implying that they formed by shearing of distorted or spherical vesicles (Gardner et al. 2017). No shear occurred in our experiments because the applied pressure is isotropic. Over 70% of the North Mono obsidians preserve stretched/elongated vesicles, indicating that most, if not all, pyroclasts underwent shearing during their formation. It is not possible to determine the cause of shearing based on available evidence, but we speculate that it could be associated with gravitational slumping of the sintering mass at the conduit wall or shearing along the margins induced by the ascent of the adjacent erupting gas-particle dispersion, either before or during the disruption of the obsidian to form pyroclasts.

Conclusions

Rhyolitic ash particles were experimentally sintered to examine the evolution of the vesicle textures that result. Results show that, regardless of particle size, porosity decreases with time and the interstitial pores quickly isolate to form vesicles amongst the sintering particles. With time, isolated vesicles that are initially highly distorted relax to spherical shapes. The rates of sintering and relaxation depend on melt viscosity and initial sizes of the particles. All else being equal, smaller particles sinter more quickly than coarser ones. We also found that high vesicle number densities ($N_v \geq 10^7$ cm^{-3}) and generally small vesicle sizes result when the sintering particles are unimodal fine-grained ash. Cooling of the sintering pack causes thermally driven resorption of volatiles, which reduces vesicle abundances below the equilibrium abundance of 3–5 vol.%, and can ultimately produce glass that is devoid of vesicles. While cooling reduces the overall porosity, it also allows distorted vesicles to be preserved for longer periods of time and to lower porosities. Finally, bimodal mixtures of coarse and fine ash result in significantly more heterogeneous vesicular textures than unimodal samples, including the creation of large pockets of large vesicles between relict coarse particles. In addition, the overall reduction of porosity and relaxation of vesicle shapes also takes longer than in unimodal samples.

These results provide a framework in which to interpret observed vesicle textures in natural obsidian pyroclasts. In general, we conclude that obsidian pyroclasts form by sintering of mostly fine-grained ash on conduit walls. The sintering ash also cools sufficiently slowly that the majority of obsidian pyroclasts have vesicle abundances well below those produced in isothermal sintering experiments. The various scales of heterogeneous vesicle abundances and volatile concentrations indicate that the sintering particle pack is not only unimodal fine ash and that some pieces of obsidian incorporated by the eruption column are re-plastered onto the walls to re-sinter with other fragments and more ash.

Acknowledgements JEG and JMW were partially supported by grants from the National Science Foundation (EAR–1725186 and EAR–1725207). EWL and JPC acknowledge support from the UK Natural Environment Research Council via grant NE/N002954/1. FBW acknowledges a fellowship from the Centre for Advanced Study at the Ludwig-Maximilians-Universität, Munich. All data from the study can be obtained from JEG. The authors thank two anonymous reviewers and the Associate Editor for their insights, which have improved the manuscript.

Appendix 1

Whether there is enough time for silicate melt to flow viscously to allow the bubbles to shrink depends on the timescale for H_2O to resorb from vesicles (λ_γ) and the characteristic time required for the melt to flow (λ_η). Both timescales are functions of solubility (C_e), diffusivity (D), and melt viscosity (η), all of which are functions of temperature (Fig. 10), and so, they change through the cooling ramp. The curves for $C_e(T)$ and $D(T)$ also require a dissolved water content to be assumed. We choose $C_{e,\,0}$, which is the initial solubility of water in the melt, in wt.%, at the start of the cooling ramp. This is the lowest dissolved water content anticipated during the experimental run. This value yields the highest viscosity and slowest diffusivity and so constitutes the most conservative assumption. In our analysis, we use the time-averaged values of each parameter over the linear cooling ramp: $\overline{C_e}$, $\overline{D}$, and $\overline{\eta}$, respectively.

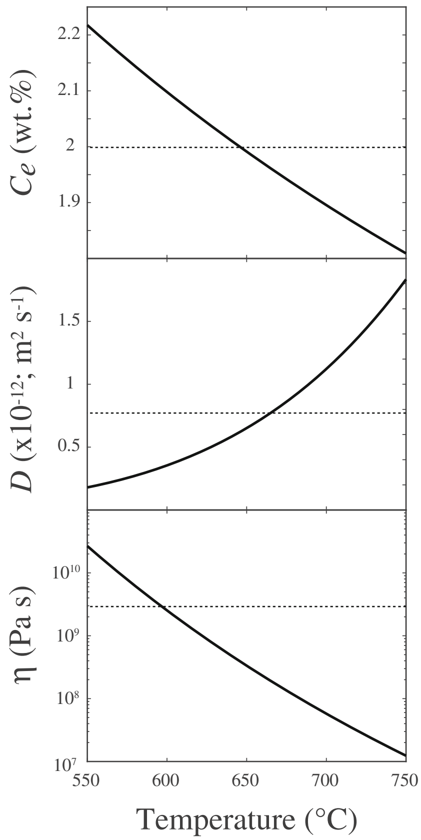

Fig. 10 Solid curves are solubility (C_e), diffusivity (D), and viscosity (η) as functions of temperature, all at 22 MPa H_2O pressure. Dash lines are time-averaged values of each during constant rate cooling from 750 to 550 °C. Diffusivity and viscosity are calculated under the conservative assumption that dissolved H_2O content is given by solubility at 750 °C

In order to estimate λ_γ, we first calculate the mass (M_0) of H_2O contained within a bubble of initial radius (R_0) at the start of the cooling ramp, using the equation of state of Pitzer and Sterner (1994). We then calculate the volume (V) of melt that would be required to resorb this mass of water:

$$V = \frac{M_o(R_o, P, T_o)}{\left[\frac{\left(\overline{C_e} - C_{e,o}\right)}{100}\rho_m\right]} \tag{4}$$

where $M_0(R_0, P, T_0)$ indicates that M_0 is a function of initial bubble radius, experimental pressure, and initial temperature (via the equation of state), and ρ_m is density of the melt, taken as 2300 kg m^{-3}. We assume that, if resorption goes to completion, then V will be a sphere of hydrated melt with radius $R_h = \sqrt[3]{3V/4\pi}$. The characteristic diffusion length scale at the end of the cooling ramp is estimated as $l_D = \sqrt{\overline{D}t}$. By setting $l_D = R_h$, we can estimate the duration of the cooling ramp required to fully resorb the water in the bubble by diffusion:

$$\lambda_\gamma = \frac{1}{\overline{D}}\left(\frac{3M_o(R_o, P, T_o)}{4\pi\rho_m\frac{\left(\overline{C_e} - C_{e,o}\right)}{100}}\right)^{\frac{2}{3}} \tag{5}$$

The characteristic time required for the melt to flow viscously to allow the bubble to collapse is estimated by assuming that it scales with the ratio of the viscosity of the melt to the stresses driving collapse, which are the surface tension (Laplace) stress σ and the confining pressure, given by

$$\lambda_\eta = \frac{\overline{\eta}}{\left(\frac{\sigma}{R_o} + P_o\right)} \tag{6}$$

References

Alfano F, Bonadonna C, Watt S, Connor C, Volentik A, Pyle DM (2016) Reconstruction of total grain size distribution of the climactic phase of a long-lasting eruption: the example of the 2008–2013 Chaitén eruption. Bull Volcanol 78:46

Bonadonna C, Houghton BF (2005) Total grain-size distribution and volume of tephra-fall deposits. Bull Volcanol 67(5):441–456

Cabrera A, Weinberg RF, Wright HMN, Zlotnik S, Cas RAF (2011) Melt fracturing and healing: a mechanism for degassing and origin of silicic obsidian. Geology 39:67–70

Castro JM, Cordonnier B, Tuffen H, Tobin MJ, Puskar L, Martin MC (2012) The role of melt-fracture degassing in defusing explosive rhyolite eruptions at Volcán Chaitén. Earth Planet Sci Lett 333-334:63–69

Castro JM, Bindeman IN, Tuffen H, Schipper CI (2014) Explosive origin of silicic lava: textural and δD–H_2O evidence for pyroclastic degassing during rhyolite effusion. Earth Planet Sci Lett 405:52–61

Dunbar NW, Kyle PR (1992) Volatile contents of obsidian clasts in tephra from the Taupo Volcanic Zone, New Zealand: implications to eruptive processes. J Volcanol Geotherm Res 49:127–145

Eichelberger JC, Carrigan CR, Westrich HR, Price RH (1986) Non-explosive silicic volcanism. Nature 323:598–602

Elam WT, Kerstein AR, Rehr JJ (1984) Critical properties of the void percolation problem for spheres. Phys Rev Lett 52(17):1516–1519

Gardner JE (2007) Bubble coalescence in rhyolitic melts during decompression from high pressure. J Volcanol Geotherm Res 166:161–176

Gardner JE, Ketcham RA (2011) Bubble nucleation in rhyolite and dacite melts: temperature dependence of surface tension. Contrib Mineral Petrol 162:929–943

Gardner JE, Llewellin EW, Watkins JM, Befus KS (2017) Formation of obsidian pyroclasts by sintering of ash particles in the volcanic conduit. Earth Planet Sci Lett 459:252–263

Gardner JE, Wadsworth FB, Llewellin EW, Watkins JM, Coumans JP (2018) Experimental sintering of ash at conduit conditions and implications for the longevity of tuffisites. Bull Volcanol 80:23

Gonnermann HM, Manga M (2005a) Nonequilibrium magma degassing: results from modeling of the ca. 1340 AD eruption of Mono Craters, California. Earth Planet Sci Lett 238(1):1–16

Gonnermann HM, Manga M (2005b) Flow banding in obsidian: a record of evolving textural heterogeneity during magma deformation. Earth Planet Sci Lett 236(1):135–147

Gottsmann J, Giordano D, Dingwell DB (2002) Predicting shear viscosity during volcanic processes at the glass transition: a calorimetric calibration. Earth Planet Sci Lett 198(3–4):417–427

Hess K–U, Dingwell DB (1996) Viscosities of hydrous leucogranitic melts: a non–Arrhenian model. Am Mineral 81:1297–1300

Jaupart C, Allegre CJ (1991) Gas content, eruption rate and instabilities of eruption regime in silicic volcanoes. Earth Planet Sci Lett 102:413–429

Kaminski E, Jaupart C (1998) The size distribution of pyroclasts and the fragmentation sequence in explosive volcanic eruptions. J Geophys Res 103(B12):29759–29779

Kertész J (1981) Percolation of holes between overlapping spheres: Monte Carlo calculation of the critical volume fraction. J Physique Lett 42(17):393–395. https://doi.org/10.1051/jphyslet:019810042017039300

Liu Y, Zhang Y, Behrens H (2005) Solubility of H_2O in rhyolitic melts at low pressure and a new empirical model for mixed H_2O-CO_2 solubility in rhyolitic melts. J Volcanol Geotherm Res 143:219–235

McIntosh IM, Llewellin EW, Humphreys MCS, Nichols ARL, Burgisser A, Schipper CI, Larsen JF (2014) Distribution of dissolved water in magmatic glass records growth and resorption of bubbles. Earth Planet Sci Lett 401:1–11

Newman S, Epstein S, Stolper E (1988) Water, carbon dioxide and hydrogen isotopes in glasses from the ca. 1340 A.D. eruption of the Mono Craters, California: constraints on degassing phenomena and initial volatile content. J Volcanol Geotherm Res 35:75–96

Okumura S, Nakamura M, Nakashima S (2003) Determination of molar absorptivity of IR fundamental OH stretching vibration in rhyolitic glasses. Am Mineral 88:1657–1662

Okumura S, Nakamura M, Takeuchi S, Tsuchiyama A, Nakano T, Uesugi K (2009) Magma deformation may induce non-explosive volcanism via degassing through bubble networks. Earth Planet Sci Lett 281(3–4):267–274

Pitzer KS, Sterner SM (1994) Equations of state valid continuously from zero to extreme pressures for H2O and CO2. J Chem Phys 101:311

Rust AC, Cashman KV (2007) Multiple origins of obsidian pyroclasts and implications for changes in the dynamics of the 1300 B.P. eruption of Newberry Volcano, USA. Bull Volcanol 69:825–845

Rust AC, Cashman KV, Wallace PJ (2004) Magma degassing buffered by vapor flow through brecciated conduit margins. Geology 32:349–352

Taylor BE (1991) Degassing of Obsidian Dome rhyolite, Inyo volcanic chain, California. Geochem Soc Spec Publ 3:339–353

Taylor BE, Eichelberger JC, Westrich HR (1983) Hydrogen isotopic evidence of rhyolitic magma degassing during shallow intrusion and eruption. Nature 306:541–545

Tuffen H, Dingwell DB (2005) Fault textures in volcanic conduits: evidence for seismic trigger mechanisms during silicic eruptions. Bull Volcanol 67(4):370–387

Tuffen H, Dingwell DR, Pinkerton H (2003) Repeated fracture and healing of silicic magma generate flow banding and earthquakes? Geology 31:1089–1092

Vasseur J, Wadsworth FB (2017) Sphere models for pore geometry and fluid permeability in heterogeneous magmas. Bull Volcanol 79(11):77

Wadsworth FB, Vasseur J, von Aulock FW, Hess KU, Scheu B, Lavallée Y, Dingwell DB (2014) Nonisothermal viscous sintering of volcanic ash. J Geophys Res 119:8792–8804

Wadsworth FB, Vasseur J, Llewellin EW, Schauroth J, Dobson KJ, Scheu B, Dingwell DB (2016) Sintering of viscous droplets under surface tension. Proc R Soc A 472(2188):20150780

Wadsworth FB, Vasseur J, Llewellin EW, Dobson KJ, Colombier M, von Aulock FW, Fife JL, Wiesmaier S, Hess KU, Scheu B, Lavallée Y (2017) Topological inversions in coalescing granular media control fluid-flow regimes. Phys Rev E 96(3):033113

Walker GPL (1981) Plinian eruptions and their products. Bull Volcanol 44:223–240

Watkins JM, Gardner JE, Befus KS (2017) Non-equilibrium degassing, regassing, and vapor fluxing in magmatic feeder systems. Geology 45:183–186

Zhang Y, Ni H (2010) Diffusion of H, C, and O components in silicate melts. Rev Mineral Geochem 72:171–225

Zhang Y, Belcher R, Ihinger PD, Wang L, Xu Z, Newman S (1997) New calibration of infrared measurement of dissolved water in rhyolitic glasses. Geochim Cosmochim Acta 61:3089–3100